



Constraining Earth's nonlinear mantle viscosity using plate-boundary resolving global inversions

Jiashun Hu^{a,1,2} , Johann Rudi^{b,1}, Michael Gurnis^c, and Georg Stadler^d

Affiliations are included on p. 8.

Edited by David Bercovici, Yale University, New Haven, CT; received November 10, 2023; accepted May 20, 2024

Variable viscosity in Earth's mantle exerts a fundamental control on mantle convection and plate tectonics, yet rigorously constraining the underlying parameters has remained a challenge. Inverse methods have not been sufficiently robust to handle the severe viscosity gradients and nonlinearities (arising from dislocation creep and plastic failure) while simultaneously resolving the megathrust and bending slabs globally. Using global plate motions as constraints, we overcome these challenges by combining a scalable nonlinear Stokes solver that resolves the key tectonic features with an adjoint-based Bayesian approach. Assuming plate cooling, variations in the thickness of continental lithosphere, slabs, and broad scale lower mantle structure as well as a constant grain size through the bulk of the upper mantle, a good fit to global plate motions is found with a nonlinear upper mantle stress exponent of 2.43 \pm 0.25 (mean \pm SD). A relatively low yield stress of 151 \pm 19 MPa is required for slabs to bend during subduction and transmit a slab pull that generates asymmetrical subduction. The recovered longterm strength of megathrusts (plate interfaces) varies between different subduction zones, with South America having a larger strength and Vanuatu and Central America having lower values with important implications for the stresses driving megathrust earthquakes.

mantle rheology | plate motion | adjoint inversion | stress exponent | activation energy

The solid Earth is a viscoelastic body, but on long geological time scales, the elastic effect can be ignored and deformation is mainly controlled by an effective viscosity. The viscosity of rocks inside the Earth is governed by different mechanisms including diffusion creep, dislocation creep, and different forms of plastic deformation which are in turn controlled by temperature, pressure, crystal size, water content, strain rate, and melt fraction (1, 2). Understanding the rheology of the solid Earth has relied on experiments, but imposed strain rates are often many orders of magnitude ($\sim 10^6$) higher than that of geological processes (3), raising concerns on the applicability of the measured values of constitutive parameters. Nevertheless, these experiments provide important constraints on rheological parameters. For example, for the bulk of the high-temperature upper mantle, the activation energy (E_a) for dislocation creep of olivine is within the range of 430 to 640 kJ/mol (4), while its stress exponent (n) is usually considered to be within 3.5 ± 0.3 (3, 4). In the localized shear zones and at subducting boundaries, the minerals can undergo grain size reductions. This favors the predominance of grain-size sensitive creep (5) in geologically recognized areas with long-term inherited weaknesses (6). The laboratory flow laws have been incorporated into regional, generic forward geodynamic models with realistic geophysical outcomes for tectonic plates and subduction zones

Alternatively, the viscous behavior of lithosphere and mantle can be inferred from geophysical observations, including those using postglacial (9, 10) and postseismic rebound (11, 12), plate motions (13-15), the gravitational field (16-19), and other phenomena as constraints. These studies can obtain the variation in effective viscosity of the mantle with depth and provide a first-order understanding of the present-day mantle viscosity. Through inference, either through formal inversion or forward models that match observations, rheologies are simplified, generally using Newtonian constitutive relations (9, 10, 17-22). However, it is long known that inferred radial variations in viscosity trade-off with lateral variations (23) and that plate tectonics is strongly governed by lateral variations in mechanical properties. There are some examples of assuming nonlinear constitutive relations in forward models that fit plate motion observations and that attempt to infer nonlinear parameters (24, 25), but there are no formal inversions with realistic nonlinear constitutive relations on a global scale.

Significance

Solid Earth evolution is regulated by mantle convection and plates that deform with highly nonlinear rheologies and with plastic failure. Geophysical inference has been unable to account for such nonlinearities while simultaneously resolving the two key tectonic elements globally: bending plates and megathrust faults. Through advancing the robustness and scalability of computational methods, and combining them with global lithosphere, slab, seismicity, and tomography data, we overcome the key challenges. We find that the nonlinearity and stress magnitude for plastic failure during mantle deformation is smaller than found in laboratory experiments while the tectonic stress delivered to different plate interfaces varies for different subduction zones with implications for megathrust earthquakes.

Author contributions: J.H. and M.G. designed research; J.H. performed research; J.R., M.G., and G.S. contributed new reagents/analytic tools; J.H. and M.G. analyzed data; and J.H., J.R., M.G., and G.S. wrote the paper.

The authors declare no competing interest.

This article is a PNAS Direct Submission.

Copyright © 2024 the Author(s). Published by PNAS. This article is distributed under Creative Commons Attribution-NonCommercial-NoDerivatives License 4.0

¹J.H. and J.R. contributed equally to this work.

 $^2\mbox{To}$ whom correspondence may be addressed. Email: hujs@sustech.edu.cn.

This article contains supporting information online at https://www.pnas.org/lookup/suppl/doi:10.1073/pnas. 2318706121/-/DCSupplemental.

Published July 5, 2024.

We advance substantially beyond previous approaches for the global problem of plate motions and associated mantle flow. Namely, we construct a model of coupled, plate boundary-resolving lithosphere-mantle deformation, use gradients based on forward and adjoint variants of the governing Stokes system of equations, and take a Bayesian inference approach. We use rheological parameters based on laboratory experimental results as prior knowledge, fit global plate motions, and approximate posterior probability distributions of the rheological parameters and the covariation between them. Unlike previous inversions, this work utilizes plate-resolving forward models, efficient inversion methods to obtain estimates of rheological parameters, and more detailed three-dimensional structure of the lithosphere and mantle, including the details of the bending oceanic lithosphere globally.

Global Derivative-Based Inversion Using Plate Motion

We use a spherical shell Ω as domain of the earth's mantle, and model its long-time dynamics using viscous non-Newtonian fluid equations for the conservation of mass and momentum, i.e.,

$$-\nabla \cdot \boldsymbol{u} = 0, \quad -\nabla \cdot \boldsymbol{\sigma} = \boldsymbol{f}_{g} \quad \text{in } \Omega.$$
 [1]

Here, \mathbf{u} is the fluid velocity and $\mathbf{\sigma} = 2\eta\dot{\mathbf{\epsilon}} - p\mathbf{I}$ is the viscous stress tensor, with η being the highly nonlinear, parameter-dependent viscosity (details below), $\dot{\mathbf{\epsilon}} = \frac{1}{2}(\nabla \mathbf{u} + \nabla \mathbf{u}^T)$ is the strain rate, and p is the pressure. The gravitational force is $\mathbf{f}_g := -\rho g \mathbf{e}_r$, where ρ denotes the density, g the gravitational acceleration, and

 \mathbf{e}_r the unit-length radial direction. Eq. **1** is complemented with free-slip boundary conditions, such that the flow is solely driven by gravitational force. Any emergence of flow or plate tectonics-like behavior is a consequence of the interaction of gravity with the nonlinear viscosity η through the solution of Eq. **1**. A typical solution of Eq. **1** is shown in Fig. 1. Simplified from experimental flow laws, the nonlinear viscosity is given by

$$\eta(\mathbf{x}, T, \dot{\varepsilon}_{\text{II}}, \mathbf{m}) = \eta_{\min} + \min \left\{ \frac{\sigma_{y}}{2\dot{\varepsilon}_{\text{II}}}, \omega(\mathbf{x}) \min \left\{ A^{1/n} \dot{\varepsilon}_{\text{II}}^{\frac{1-n}{n}} \right\} \right\}$$

$$\times \exp \left(\frac{E_{a} \Delta T}{nRT_{m}^{2}} (1 - T) \right), \eta_{\max} \right\}. \quad [2]$$

Here, η_{\min} and η_{\max} are lower and upper bounds for the viscosity; σ_y is the yield stress; $\dot{\epsilon}_{\text{II}}$ is the square root of second invariant of the strain rate tensor; A is viscosity scaling, with A_u for upper mantle and A_l for lower mantle; n is the stress exponent; E_a is the activation energy; R is the gas constant that equals 8.314 kJ/mol; ΔT is the temperature difference between the surface and the mantle that equals 1,400 K; T_m is the mantle temperature equal to 1,673 K; $T=(T-T_s)/\Delta T$ is the nondimensional temperature field where $T_s=273$ K is the surface temperature; and $\omega(\mathbf{x})$ is the extra weakening along the plate boundaries (Fig. 1C), which involves parameters $\omega_i \in \mathbb{R}$ that control the coupling between individual plates.

The constitutive relation adopted (Eq. 2) is simplified, perhaps most significantly in dropping the dependence on grain size which acts as a nonlinear term for diffusion creep when grain size evolves (5). This simplification is likely most significant within the shear zones between plates; here the shear zones

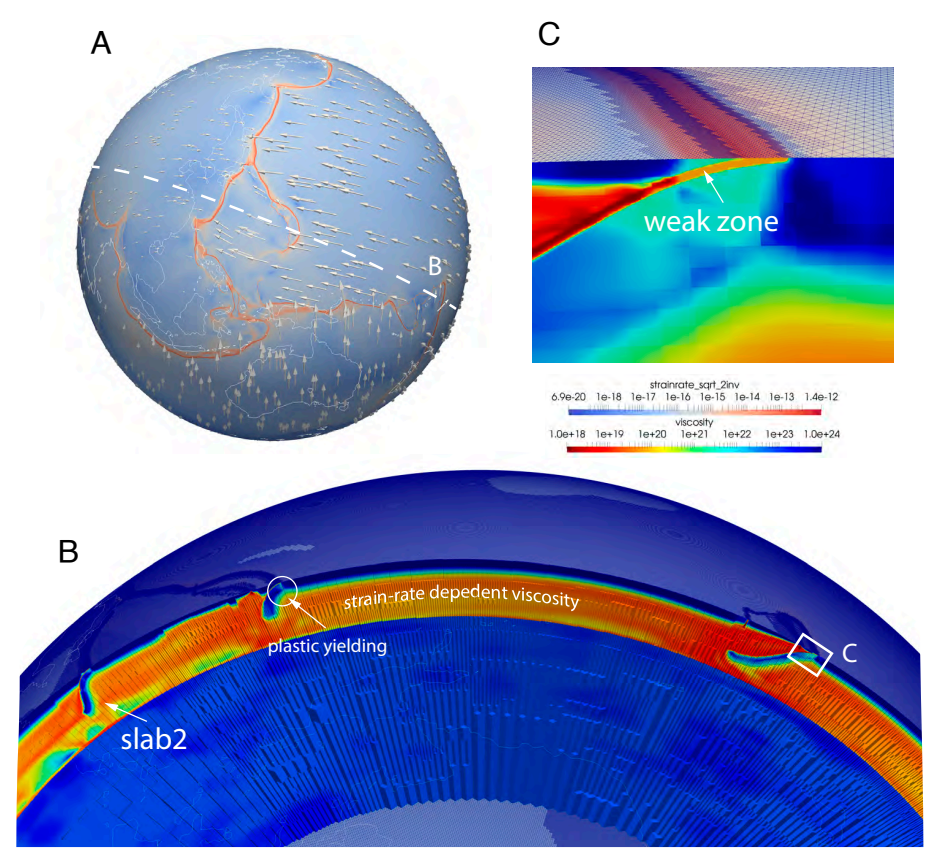


Fig. 1. Setup of the global forward Stokes solver. (A) Global view of strain rate and plate motion on the surface. (B) Cross-section showing the viscosity field and the computational mesh along a profile shown in (A). (C) Enlarged view of the subduction zone showing the detailed structure of the bending lithosphere and the weak zone.

could be peridotitic mylonites with much reduced grain sizes with a dominance of diffusion over dislocation creep (26, 27). Grain evolution and creep processes can be incorporated into forward, generic models of subduction (28), but these require that strain evolves forward in time, which cannot be attained in instantaneous Stokes; consequently, assuming these shear zones have strain-inherited rheologies, we have approximated them with a set of local parameters, ω_i , in addition to the creep parameters, E_a and n, which act within the entirety of the upper mantle.

The thermal field T is the combination of the lithosphere defined using the half-space cooling model with magnetic anomaly-constrained plate ages (29), slabs based on the slab2 model (30), variations in the thickness of continental lithosphere, and lower mantle structure converted from seismic tomography (31) (*Materials and Methods* and *SI Appendix*, Fig. S1). For the inversion, the MORVEL56 plate model in the no-net-rotation (NNR) reference frame (32) is the data used as surface velocity field; this model was selected because of the inclusion of major and minor plates allowing us to exploit the strength of the computational models, which resolve the fine details of plate margins, including the microplates that display back-arc motion. As the inversions were computed with data in a NNR frame, they cannot be used to address the origin of net rotations, as considered in forward models (22, 33, 34).

When solving Eq. 1, it is essential to use adaptive mesh refinement to resolve crucial small-scale structures (Fig. 1 *B* and *C*), especially the plate boundaries for different subduction zones. Using discretizations with local resolution of 1 km is needed to resolve subduction zone dynamics. Despite the use of locally highly adapted meshes, discretization of Eq. 1 typically results in extremely large (i.e., hundreds of millions of unknowns) nonlinear implicit system, requiring tailored parallel solvers (35, 36) on large supercomputers (37).

The vector **m** on the left-hand side of Eq. **2** includes uncertain parameters from the right-hand side that play a crucial role for the viscosity: the yield stress σ_{γ} , the stress exponent n, the activation energy E_a in the upper mantle, the upper and lower mantle scalings A_u and A_l , and the weak zone factors ω_i at major subduction zones. Each choice of m results in a different surface flow. The main purpose of this work is to show that it is possible to use global plate tectonic data to constrain these parameters, and to study trade-offs between them. Such a systematic parameter inference approach extends previous studies (38, 39) to global models, building on related high-resolution forward model studies (25, 40, 41). We formulate this parameter inference problem as Bayesian inference for the viscosity parameters m. Besides the ability to solve Eq. 1, such a study is facilitated by the availability of derivatives with respect to the parameters m of the misfit between the model output and present-day tectonic data. We compute these derivatives efficiently using adjoint methods (Materials and Methods). This allows us to compute the maximum a posteriori (MAP) parameters using gradient-based optimization, and to find covariance matrix approximations that provide information about the uncertainty of the estimated parameters. An alternative to gradient-based inference are Monte Carlo sampling methods, as illustrated with simpler low-dimensional models (38, 42), which would require a large number of solves of Eq. 1 for different parameters m. Given that a single high-resolution solve may require hours on several thousand central processing unit (CPU) cores, such samplingbased methods are infeasible.

Results

The MAP point optimization converges close to observed plate motions while exhibiting behavior widely found in highresolution forward models of subduction zones in 2-D crosssections (e.g., 7). The oceanic lithosphere gradually bends within the hinge zone below the low viscosity megathrust (Fig. 1C) while the hinge zone itself yields. Throughout the interior of plates, the strain rates are low and less than about $10^{-17}\ s^{-1}$ with high values directly above megathrusts. The slabs below the hinge zone have high viscosities, although limited by an imposed maximum value, the viscosities still show considerable variation between subduction zones. The high viscosities allow the slabs to act as stress guides. The regions around slabs, including within the mantle wedge are characterized by halos of low viscosities generated by shear thinning. The values of the viscosities within hinge zones, slabs, and the upper mantle are determined by the combination of tectonic plate data and the governing Stokes and constitutive equations.

Fit to Plate Motions. Using plate motion as constraints, the parameters in the viscosity law (Eq. 2) are recovered. Given the initial guess on them, where $A_u = 2.81 \times 10^{10}$ (dimensional value of $1.7 \times 10^{31} \text{ Pa}^n$ -s), $A_l = 340$ (dimensional value of $3.4 \times 10^{22} \text{ Pa-s}$), $E_a = 540 \text{ kJ/mol}$, n = 3.5, $\sigma_y = 160 \text{ MPa}$, a forward solve generates surface plate speeds that are substantially larger than those observed. These initial values are also used as the mean of the prior in the Bayesian approach. At iteration 3, the plate speeds adjust themselves to be significantly lower than the observed (Fig. 2A), but the misfit decreases. The fit improves gradually with each descent step in the MAP parameter optimization, so that by iteration 26, the predicted plate motions generally match that observed both in orientation and magnitude (Fig. 2B), while also fitting the motions of microplates such as for the North Fiji and Lau Basins associated with Vanuatu and Tonga Trench rollback (SI Appendix, Fig. S2). The optimization is reasonably converged by this iteration, given the slowdown in reduction to the objective function after iteration 10 and the reduction of the gradient norm of the objective compared to the initial value indicating a minimum has been reached (SI Appendix, Fig. S3). Some misfit exists though, such as for the Nazca and Australian Plates, and might indicate model errors or imperfect knowledge on the mantle structure that drives plate motion in these regions, as discussed later.

The final iteration produces a stress exponent $n = 2.43 \pm 0.25$ (where all uncertainties assigned to the posterior are one SD), a yield stress $\sigma_y = 151 \pm 19$ MPa, and an upper mantle activation energy $E_a = 648 \pm 70$ kJ/mol (Fig. 3 A–C). Other calculations suggest that this is not a local minima but rather a global one, as considered in the discussion below. A computation that started with a substantially different initial guess compared to the prior mean—no strain-rate weakening (n being 1.0 instead of 3.5), a much higher yield stress (σ_y being 320 MPa instead of 160 MPa) and a higher activation energy (E_a being 810 kJ/mol instead of 540 kJ/mol) (SI Appendix, Figs. S3-S5) returns a posterior distribution close to the reference case just described. In this case, the recovered strain-rate weakening, yield stress, and activation energy only slightly changed (n changing from 2.43 ± 0.25 to 2.42 ± 0.26 , σ_{γ} from 151 ± 19 MPa to 142 \pm 17 MPa and E_a from 648 \pm 70 kJ/mol to 661 ± 71 kJ/mol). This suggests the robustness of the inversion results.

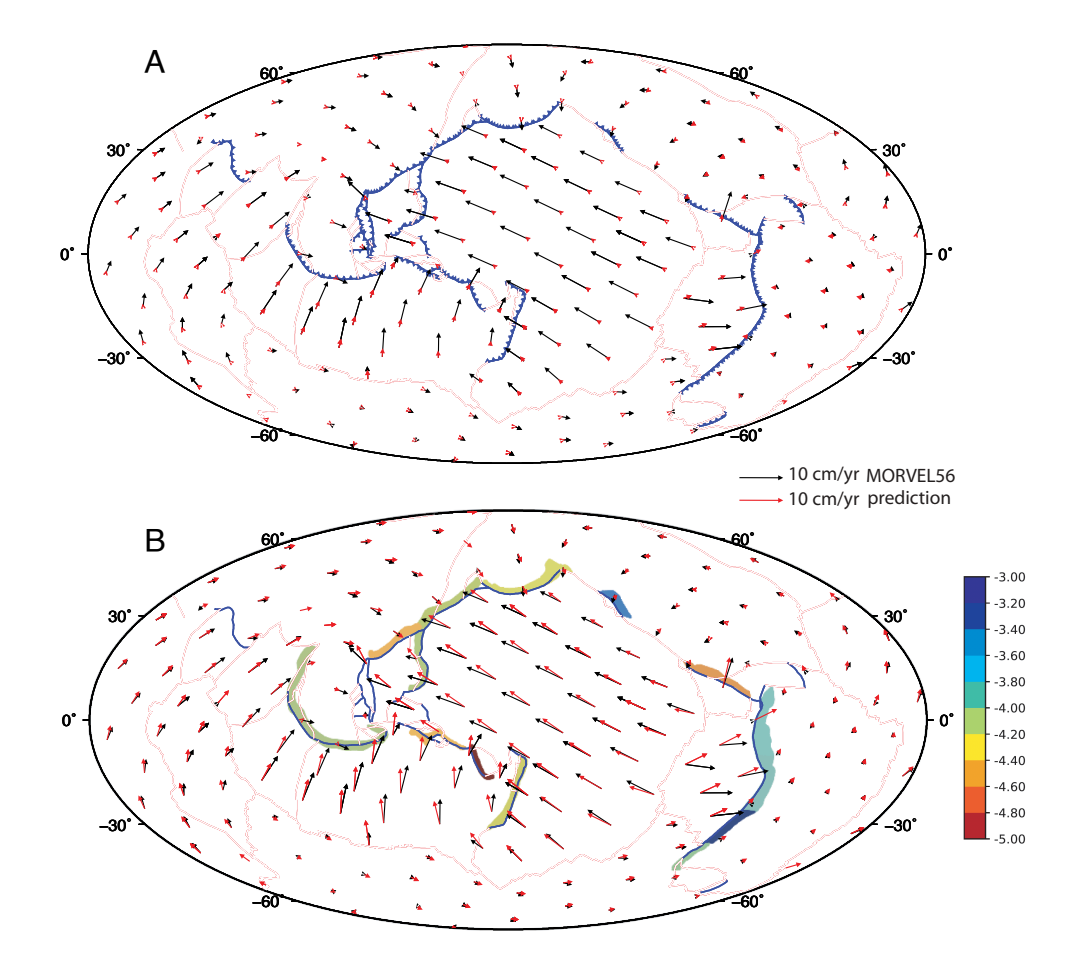


Fig. 2. Plate motions at iteration 3 (*A*) and 26 (*B*) of adjoint inversion. Red arrows represent predicted velocities by the geodynamic model, while black arrows represent the data model MORVEL56 constrained by geophysical observations (43). The background color in (*B*) shows the inverted weak zone factors, $\log_{10}(\omega_i)$, for major subduction zones. For the rest of subduction zones, the slabs are short and we simply assume they are fully decoupled with a weak zone factor of 10^{-5} .

Inferred Parameters. As the fit to plate motions gradually improve during optimization, significant differences are found in the parameter values compared to the initial guesses and the prior means. Both the upper mantle scaling and the yield stress drop (Fig. 3A and SI Appendix, Fig. S3B), which can reduce the viscosity in the mantle and within the slabs, and increase the speed of plate motions. In contrast, the lower mantle scaling and upper mantle activation energy increase (Fig. 3 B and C). The change in E_a is complicated because increased values lead to higher slab viscosities which increase resistance to plate velocities in two ways. The first is through resistance to bending and second, for slabs that reach the lower mantle, slabs can act as more effective stress guides between the hinge zone and the higher viscosity lower mantle. In contrast, for short slabs that do not reach the transition zone, the higher E_a leads to more slab pull which could increase plate velocities. These counteracting changes in parameters indicate the strong nonlinearity of the combined system of Stokes and constitutive equations. The different effects balance in order to fit the observed asymmetry of subduction, that is, the subducting plate velocities for the Pacific, Indian, and Nazca Plates are much higher than that for overriding plates such as the Eurasian, North American, and South American plates

The marginals of the posterior distributions for the global rheological parameters show well-understood trends. The yield stress and stress exponent trade-off and are mildly correlated (Fig. 3A). A higher yield stress is needed when the stress exponent

increases as both contribute to the nonlinearity in the effective viscosity. The activation energy and stress exponent are also positively correlated (Fig. 3B) as a higher stress weakening is required when the strength of the temperature dependence to viscosity increases.

The weak zone factors at subduction zones control the strength of the plate interface and exert an important influence on plate motion. Besides the globally constant parameters, the optimization simultaneously adjusts each subduction weak zone factor, ω_i , with a prior mean (10⁻⁴, Fig. 2*A*). The inferred weak zone factors vary for different subduction zones, with the values generally ranging between 10^{-5} and 10^{-3} (Fig. 2*B*). Some subduction zones have larger weak zone factors, such as the South American subduction zones in Chile and Peru which are between $10^{-3.8}$ and $10^{-3.0}$ (Fig. 3F) while also having some of the highest tangential stresses along the megathrust (78 MPa, Table 1). Some have lower weak zone factors, including those for Mexico and Central America (between 10^{-4.6} and 10^{-4.5}) and with smaller megathrust shear stresses (about 7.9 MPa). For nearly all weak zone factors, including for those in South and Central America, as just discussed, there is not a simple trade-off between nonlinear stress exponent and weak zone factor as weak zone factors are localized parameters and n is global; the same holds true for margins of weak zone factors versus yield stress (SI Appendix, Fig. \$6) . However, the outcomes for Tonga and Kermadec (with the label KER) deviate from this assertion. In this case, we find weak zone factors which are intermediate in

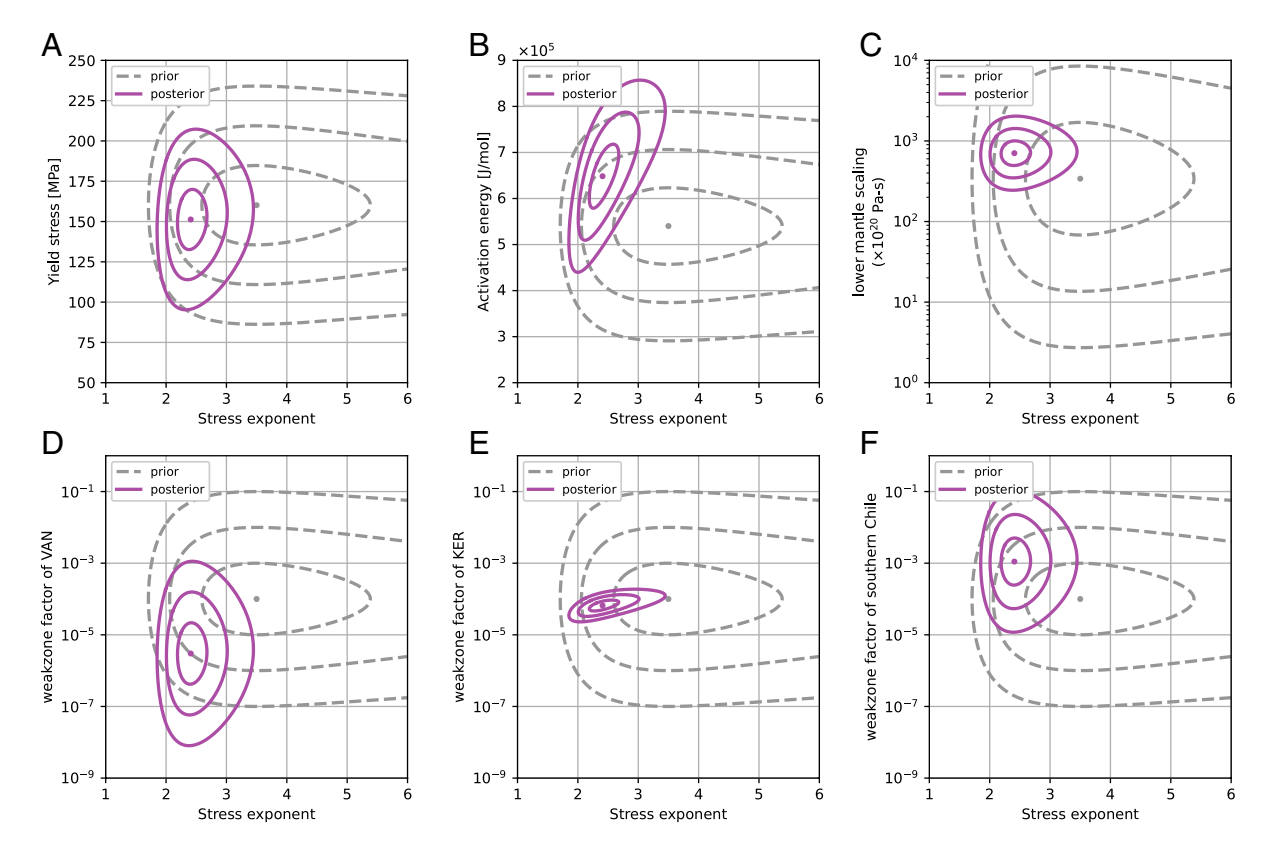


Fig. 3. Prior and posterior 2D marginal distribution of yield stress (*A*), activation energy (*B*), scaling in lower mantle (*C*), weak zone factors of Vanuatu (*D*), Tonga and Kermadec (*E*), and Southern Chile (*F*) versus stress exponent. Gray dashed lines present the prior distribution, while the solid purple lines present the posterior distribution. Each contour indicates one SD of the distribution, with the center point indicating the maximum a posteriori point.

magnitude $(10^{-4.2} \text{ to } 10^{-4.1})$ and with intermediate shear stress (7.6 to 21 MPa). However, most notable is that the variance on the logarithm of the weak zone factor (with a value of 0.152) is

Table 1. Mean deviatoric stresses along cross-sections and in the depth range of 10 to 50 km for different subduction zones

Name	Slab2	Lon(°)	Lat(°)	$\log_{10}(w_i)$	$\sigma^{(t)}$ (MPa)
Central Aleutians	ALU	-176.5	50.5	-4.23	19.8
E. Aleutians	ALU	-155.7	55.3	-4.23	16.4
Alaska	ALU	-146.2	60	-4.23	13.5
Central America	CAM	-88	10.7	-4.53	7.9
Mexico	CAM	-98.9	15.9	-4.53	7.9
Cascadia	CAS	-125.6	43.6	-3.47	24.4
Mariana	IZU	147.3	18.7	-4.06	21.4
Izu-Bonin	IZU	142.7	29.4	-4.06	19.8
N. Tonga	KER	-173	-16.2	-4.18	7.6
S. Tonga	KER	-177.5	-31.2	-4.18	21.0
Honshu	KUR	143.9	38.4	-4.10	38.7
Kamchatca	KUR	160.8	51.9	-4.10	28.0
Kuriles	KUR	152.2	45.3	-4.10	40.3
Nankai/Tokai	RYU	138.7	33.8	-4.44	9.8
Ryukyus	RYU	131.1	28.9	-4.44	14.1
Central Chile	SAM	-74.1	-35.9	-2.95	78.3
South Peru	SAM	-73.1	-17.8	-3.82	28.9
Columbia-Ecuador	SAM	-80.6	1.1	-3.82	22.9
Sumatra	SUM	97.3	-0.7	-4.03	18.3
Vanuatu	VAN	167.4	–17.9	-5.52	1.4

Shown in the table are the coupling factors w_i and $\sigma^{(t)}$, the stress tangential to the plate interface for various subduction zones.

substantially smaller than all other plate boundaries in which we find a positive trade-off between ω_i and n (Fig. 3E).

Discussion

To study if the computed MAP points correspond to global or just local minima, we use two geographically global 3-D inversions of the current work, and we discuss these in the context of a larger number of 2-D inversions (38, 39), where the smoothness and uniqueness of inverted parameters for the nonlinear Stokes system were studied. With the geographically global models, we performed an additional inference experiment with different initial guesses on n (1 versus 3.5), E_a (540 kJ/mol versus 810 kJ/mol), and σ_y (160 MPa versus 320 MPa). We only find minor differences in the posterior distributions with these vastly different initializations. These differences are most likely caused by numerical errors in the derivative computation, rather than local minima in the MAP computation.

We can also place these global inversions in the context of results from 2-D models. One set of two-dimensional models used cross-sections through the Pacific (39) and the other Cartesian sections with known rheological parameters and synthetic data (38). If different initial guesses are chosen and the same data were used as constraints, the inversion settles on the same final MAP point: For different values of n between 2.0 and 3.2, the inversions converge to n = 2.8 for the Pacific cross-sectional models (39). In the case of the 2-D Cartesian models, different guesses to the coupling factors, ω_i , were made but with the same prior knowledge with models converging to the same known values of n, σ_y , and ω_i (38). Equally important, repeated forward solves (of the nonlinear

Stokes system) were made with a Markov chain Monte Carlo (MCMC) method allowing the computational approximation of general posterior distributions without the solution being approximated by a Gaussian (as done in the current work). The resulting MAP points and covariance approximations closely approximated the actual (MCMC-computed) posterior marginal distributions and no local (or spurious) minima were found. Overall, the Gaussianity of the MCMC-computed posterior distributions was qualitatively similar to those found here (Fig. 3). Significant deviations from a Gaussian were only found when plate margins were allowed to be more deformable (38) or when data noise increased (38) that different values of the rheological parameters were recovered. Consequently, the evidence suggests that the solutions of the current work converge to global rather than local minima of the rheological parameters.

This inversion involves several assumptions, including constant grain size through the bulk of the mantle, the exclusion of high-temperature anomalies in the upper mantle and a simple conversion coefficient from tomography to density anomalies (Materials and Methods). The adoption of these assumptions is a compromise due to our incomplete knowledge of the mantle structure. However, even with these assumptions, we find the inversion results are broadly consistent with laboratory experiments. For example, our methods provide constraints on the stress exponent of the upper mantle, with a value of $n=2.43\pm0.25$ (Fig. 3A). This stress exponent is notably smaller than those constrained by laboratory experiments that suggest values of 3.0 (4), 3.5 ± 0.3 (3), and 3.6 ± 0.24 (44) for wet olivine and values of 3.5 (4) and 3.5 ± 0.3 (3) for dry olivine. None of these values is preferred, but neither can they be excluded as values of n up to 3.5 are within three SDs of the recovered posterior distributions (Fig. 3). Using a statistical framework in which experimental uncertainties are taken into account suggests that *n* for dry olivine could be as high as 4.49 ± 0.05 or even more (44). Such large values of n lead to extreme degrees of shear thinning and seem unlikely based on the global inversions. The recovered values of n trade off with the activation energy E_a (Fig. 3B). The inferred activation energy of 648 ± 70 kJ/mol is higher than those constrained by earlier laboratory experiments that suggest a value of 430 kJ/mol (4) or 480 ± 40 kJ/mol (3) for wet olivine and a value of 540 kJ/mol (4), 530 ± 4 kJ/mol (3) for dry olivine, but overlaps in range with those suggesting a value of 523 ± 100 kJ/mol (44) and 610 ± 30 kJ/mol (44), respectively for wet and dry olivine. Activation energies smaller than 400 kJ/mol are excluded by the global inversion at three SDs. As such, none of the experimental values for activation energy under dislocation creep can be excluded.

Broadly speaking the recovered n and E_a paint a picture in which shear thinning is smaller and the influence of the temperature dependence of viscosity is larger than predicted experimentally for dislocation creep for either dry or wet olivine. This suggests a stronger effective temperature dependence (larger E_a/n) than the experimentally determined dislocation creep. A straightforward explanation is that the mantle is dominated by a mixture of dislocation and diffusion creep. For this case, a positively correlated set of outcomes between n and E_a is expected and would seem to be consistent with the positive correlation found (Fig. 3B). In addition, diffusion creep has a much larger effective temperature dependence (E_a/n) of viscosity than dislocation creep, as its activation energy is considered within the range of 200 to 400 kJ/mol (3, 4, 44) and n = 1. A mixture of dislocation creep with diffusion creep would bring the effective temperature dependence in between the values for

diffusion and dislocation creep individually, consistent with the inferred value of $E_a/n \approx 269 \, \mathrm{kJ/mol}$.

This trade-off between E_a and n raises the question whether it is the same as found in thermal convection with realistic rheological laws (45). In fully developed thermal convection (e.g., through the coupling of energy and Stokes equations) with only temperature-dependent viscosity, the upper boundary tends to stagnate and the convective velocities and strain rates decrease within the cold regions (46); when shear thinning is added to the T-dependence, those viscosity variations tend to be homogenized and the range of viscosity variations decreases (45). Qualitatively similar behavior was found with the trade-off between E_a and n in the current inversion (combining nonlinear instantaneous Stokes and present-day velocity data), but it does not represent the full convection problem. Finding E_a and nand their trade-offs from an inversion against the evolution of the earth (including the history of plate kinematics) would represent such a full convection approach but also a formidable computational challenge using current technology (47).

The inferred yield stress of 151 \pm 19 MPa is substantially smaller than values found from experiments on rocks when considering Byerlee's law (48, 49). It is important to emphasize that in comparison with other global models, e.g., refs. 50-53, our computations are sufficiently well-resolved that the bending slab is distinguished from sliding between the two plates within the megathrust (e.g., Fig. 1 C). Consequently, the conclusion that the low yield stress reflects what is occurring within the hinge zone would seem to be a quite conservative one. The low yield stresses are required for slabs to bend and subduct, confirming earlier computational models of spherical convection with plates with yield stresses lower than expected by Byerlee's law (51, 52). The discrepancy between geophysical inversion and laboratory experiments on the yield stress can be explained by extra softening of the bending slab, including mantle serpentinization through water percolation along normal faults at the outer rise (54, 55) or grain size damage as the slab bends (28). Although slab softening mechanisms cannot be included in our global-scale instantaneous models, the inversion result of a low yield stress indicates that a low effective viscosity (on the order of 10²² Pa-s or less) for the slab hinge is required to fit plate motion (SI Appendix, Fig. S7).

One important contribution of this study is the inversion of the 3D mantle viscosity, especially the fine structures within subduction zones (Fig. 1B). There is considerable uncertainty regarding the strength of slabs once they pass through the hinge zone (15). The effective viscosity of slabs is a balance between strengthening through temperature dependence of viscosity (i.e., E_a) and weakening through dislocation creep and yielding (i.e., nand σ_{γ}) but all three of these parameters trade off with one another to maximize the fit to plate motions. The effective viscosity of each subducted slab adjusts during the optimization and we find considerable variation in effective viscosity and strain both between subduction zones and with depth (SI Appendix, Fig. S7). In the hinge zone, initially as the plate begins to bend (and just below the outward tip of the megathrust), we find the most variations in effective viscosity, from Vanuatu and Tonga and Kermadec on the low end with values of about 10²¹ Pa-s, through values of 10^{22} Pa-s for most subduction zones, to nearly the highest value of about 8×10^{22} for southern Chile. In contrast, the deeper part of the slabs, including for slabs that dangle in the upper mantle, like Vanuatu and Central America, or for slabs which are embedded into the transition zones, like Honshu, we find more uniform higher slab effective viscosities with values being about

10²⁴ Pa-s. The high values for Honshu are interesting because we find some trade-off in the posterior distribution between the pre-exponent of the lower mantle viscosity and the activation energy, with slightly smaller values of the pre-exponent with high E_a , reinforcing the hypothesis that the viscosity of the lower mantle is an important regulator of plate velocities in the limit of high viscosity slabs which act as stress guides. Estimates of the relative viscosity of slabs with respect to surrounding mantle vary widely: $1 \times \eta_{tz}$ (56), 100 to 300 $\times \eta_{um}$ (57), 300 $\times \eta_{um}$ (15), 500 to 2,000 \times η_{um} (58), and even higher (7) (where η_{um} and η_{tz} , are the average viscosities in the upper mantle and transition zone). The lowest estimates are from time-dependent flow models that match the shape of seismically resolved Farallon Plate fragments (56), while the others are mostly from timeindependent arguments. The inverse, global flow models have viscosity contrasts on the high end of this range, >1,000 × η_{um} , and with high absolute values for the effective viscosity of slabs, 10²⁴ Pa-s.

There is a tendency for those subduction zones with more rapid back-arc basin extension, like Vanuatu and Tonga, to have slabs with lower effective viscosity in hinge zones. However, this is not found everywhere as the Marianas has a more nominal hinge zone viscosity of 10^{22} Pa-s. This lower degree of weakening could be caused by smaller amount of trench rollback on the Marianas compared to Tonga; although the Marianas has substantial back arc extension, this is primarily caused by the westward pulling of the West Philippine Sea (59).

Of all of the plate boundaries, the variance on the inferred weak zone factor, ω_i , for Tonga and Kermadec is about an order of magnitude lower than all others. Instead of a variance of more than one magnitude we find a value of about two with a small positive trade off between ω_i and n. The kinematic constraints on Tonga are much tighter than nearly all other subduction zones. For Tonga (with fits to the local kinematics shown in *SI Appendix*, Fig. S2), the rapid rollback velocity for these systems places a direct constrain on the rate at which the plate bends in the hinge zone. So, we have very good constraints placed on the viscosity of this plate boundary that are not obtained when only kinematics of the largest plates are used as constraints on the viscosity of the hinge zone (e.g., ref. 60).

Trade-offs may exist between the input mantle density structure and the inverted viscosity parameters. For example, we assume a constant conversion coefficient from seismic velocity to density anomalies, despite that this coefficient may vary with depth and is subject to large uncertainties (61). This conversion coefficient is expected to trade off with the lower mantle viscosity. While we had to limit the systematic exploration of these uncertainties because of the features of the current inversion scheme and computational cost, we have examined some of these uncertainties using forward models. For example, we replace the lower mantle structure converted from the Pwave seismic tomography LLNL-G3Dv3 (31) with that from the S-wave tomography S40RTS (62) assuming a conversion coefficient of $dln\rho/dlnV_s = 0.2$ as widely adopted in geodynamic models (e.g., ref. 63). The predicted surface plate motion fits the observation equally well, as compared to the inversion (SI Appendix, Fig. S8). This suggests that the inverted viscosity parameters are compatible with both mantle structures.

There is also a considerable debate on whether the low seismic velocity anomalies in the upper mantle are thermal or thermochemical in origin. We have omitted these anomalies when constructing the upper mantle density structure. Therefore, the inverse model here can be taken as an end-member case where these anomalies are treated to be neutrally buoyant. However,

we have examined the influence of these upper mantle anomalies using two forward models (*SI Appendix*, Fig. S9). The predicted plate motion with the high-temperature anomalies converted from these low seismic velocity anomalies remains largely similar to the prediction without these hot anomalies, except that the Pacific Plate mildly speeds up. This is because large amounts of slow anomalies exist in South Pacific (64). This suggests that the buoyancy effect of these anomalies may not dramatically distort the inversion results, given the small change in plate motion with a nonlinear rheology. However, trade-offs may exist between the viscous effect of these low seismic velocity anomalies and the strain-rate dependency of viscosity, as they have a similar influence in reducing the effective viscosity beneath ocean basins. Given the uncertainties in the nature of these anomalies, we will rely on future studies to investigate this trade-off.

Some misfits in the mean plate motion remain even though convergence is reached for the inversion, for example within the Nazca and Australian Plates. They may reflect inadequacy of the governing equation model, or imperfect knowledge in the subduction zone structure (Fig. 2B). For the Australian plate, the weak zone factor of the Himalaya-Tibet collision zone has not been inverted for because the underlying slab structure is not well constrained, as suggested by the large inconsistency among tomography models (65-68) and with the Slab2 model (30). We used a weak zone factor with 10^{-3} in order to induce a strong resistance for continental collision, but this resistance force might be exaggerated such that it slows the Australian Plate toward the north. The misfit in the Nazca Plate remains puzzling. When the two weak zone factors for the South American subduction zone are manually adjusted in forward models, the fit in Nazca Plate is improved, but fit to the Andes and the South American Plate kinematics worsens. This could be caused by the poorly resolved slab structure in southern Chile in the Slab2 model. A longer slab may exist in this region that could increase the slab pull on the Nazca Plate in the southern part and improve the fit with the Nazca Plate (Fig. 2*B*).

Materials and Methods

Temperature Field and Viscosity. The data field T in Eq. $\bf 2$ is defined using the half-space cooling model that takes the normal age of the oceanic lithosphere (29) and assumes an age of 75 Ma near the subduction zones, an age of 300 Ma for the cratons, and an age of 125 Ma for the remaining continental lithosphere. We construct the upper mantle slabs based on the slab2 model (30) and the lower mantle density structure converted from the Lawrence Livermore National Laboratory seismic tomography (31) using a constant conversion coefficient of $d\ln\rho/d\ln V_{\it p}=0.5$ which is an approximation of the results from ref. 61. The weakening factors $\omega({\bf x})$ in Eq. $\bf 2$ along the plate boundaries (Fig. 1 $\it C$) are defined as

$$\omega(\mathbf{x}) = \prod_{i} 1 - (1 - \omega_i) \chi_i(\mathbf{x}),$$
 [3]

with $\chi_i(\mathbf{x}) = \exp(-\frac{\max\{0, \operatorname{dist}(\tau_i, \mathbf{x}) - d\}^2}{2b^2})$, where $\omega_i \in (0, 1]$ is the weak zone factor for subduction zone i, $\operatorname{dist}(\tau_i, \mathbf{x})$ defines the minimal distance between \mathbf{x} and the center surface of the weak zone τ_i , d is the width of the zone of full weakening, and b is the length-scale of smoothing. With the definition Eq. $\mathbf{2}$ as viscosity, we ensure that the slab forms a coherent structure that can transmit stress from the deep mantle to the plate on the surface, and can easily bend due to plastic yielding at the hinge zone.

Bayesian Inference Formulation. The observational data \mathbf{d}_{obs} are plate velocities at the top surface of the mantle, given by Euler poles (43). We compare the corresponding plate velocity data with velocities obtained from solving Eq. $\mathbf{1}$ in regions sufficiently far away from plate boundaries. We do not include velocity

near margins, including in the vicinity of oceanic trenches, because there the plates bend and deform, which is not captured by Euler poles. The Bayesian inference formulation incorporates a prior distribution for the parameters \mathbf{m} and a distribution of the data misfit $f(\mathbf{m}) - \mathbf{d}_{\text{obs}}$. Here, f is the map from parameters \mathbf{m} to the predicted observation data. Each evaluation of f requires solution of the nonlinear Stokes equations Eq. 1. The prior and error distribution are chosen as multivariate Gaussians with means \mathbf{m}_0 and $\mathbf{0}$ and covariance matrices C_{prior} and C_{data} , respectively. In our inversions, these covariance matrices are diagonal, i.e., C_{prior} contains the parameter variances on the diagonals, and C_{data} the data error variances. The data error variances are either chosen to scale as reciprocals of the plate area, or the square root of plate area. The latter choice gives smaller plates a comparably stronger influence on the inferred rheological parameters (39), but it apparently does not influence the relative rankings of the means of ω_i substantially (*SI Appendix*, Fig. S10). For the inversions presented here, this latter weighting is used.

The posterior distribution of \mathbf{m} given \mathbf{d}_{obs} is then given by

$$\pi_{\text{post}}(\mathbf{m}) \propto \exp(-J(\mathbf{m})),$$
 [4]

where " \propto " means equal up to a multiplicative normalization constant, and $J(\mathbf{m})$ is defined as

$$J(\mathbf{m}) := \frac{1}{2} (\mathbf{d}_{obs} - f(\mathbf{m}))^{T} C_{data}^{-1} (\mathbf{d}_{obs} - f(\mathbf{m})) + \frac{1}{2} (\mathbf{m} - \mathbf{m}_{0})^{T} C_{prior}^{-1} (\mathbf{m} - \mathbf{m}_{0}).$$
 [5]

Since evaluation of f requires the computationally expensive solution of Eq. 1, it is not feasible to fully explore the posterior distribution. We thus approximate the posterior distribution with a Gaussian, by linearizing f at the MAP point \mathbf{m}_{map} , i.e., the parameter vector minimizes $J(\mathbf{m})$. The resulting Gaussian has the mean \mathbf{m}_{map} and a covariance matrix $(\mathbf{F}C_{\text{data}}^{-1}\mathbf{F} + C_{\text{prior}}^{-1})^{-1}$, which is the inverse of the Hessian of J, where \mathbf{F} is the linearization of f. Even for diagonal C_{data} , C_{prior} , the posterior covariance is in general not diagonal as the physics leads to correlation between the parameters \mathbf{m} .

- 1. G. Ranalli, Rheology of the Earth (Springer Science & Business Media, 1995).
- S. Karato, Deformation of Earth materials: An Introduction to the Rheology of Solid Earth (Cambridge University Press, 2008), pp. 123–167.
- G. Hirth, D. Kohlstedf, Rheology of the upper mantle and the mantle wedge: A view from the experimentalists. Geophys. Monogr. Am. Geophys. Union 138, 83-106 (2003).
- 4. S. Karato, P. Wu, Rheology of the upper mantle: A synthesis. Science 260, 771–778 (1993).
- D. Bercovici, Y. Ricard, Plate tectonics, damage and inheritance. *Nature* 508, 513–516 (2014)
- M. Gurnis, S. Zhong, J. Toth, "On the competing roles of fault reactivation and brittle failure in generating plate tectonics from mantle convection" in *The History and Dynamics of Global Plate Motions, Geophysical Monograph*, M. A. Richards, R. Gordon, R. van der Hilst, Eds. (Am. Geophys. Un., 2000), vol. 121, pp. 73–94.
- M. I. Billen, G. Hirth, Rheologic controls on slab dynamics. Geochem. Geophys. Geosyst. 8, Q08012 (2007).
- M. D. Behn, G. Hirth, J. R. Elsenbeck, Implications of grain size evolution on the seismic structure of the oceanic upper mantle. Earth Planet. Sci. Lett. 282, 178–189 (2009).
- 9. L. M. Cathles, Viscosity of the Earth's Mantle (Princeton University Press, 2015).
- J. X. Mitrovica, A. M. Forte, A new inference of mantle viscosity based upon joint inversion of convection and glacial isostatic adjustment data. Earth Planet. Sci. Lett. 225, 177–189 (2004).
- J. Deng, M. Gurnis, H. Kanamori, E. Hauksson, Viscoelastic flow in the lower crust after the 1992 Landers, California, earthquake. Science 282, 1689–1692 (1998).
- Y. Hu et al., Asthenosphere rheology inferred from observations of the 2012 Indian Ocean earthquake. Nature 538, 368–372 (2016).
- T. W. Becker, R. J. O'Connell, Predicting plate velocities with mantle circulation models. Geochem. Geophys. Geosyst. 2, 1060 (2001).
- A. Forte, W. Peltier, A. Dziewonski, Inferences of mantle viscosity from tectonic plate velocities. Geophys. Res. Lett. 18, 1747-1750 (1991).
- B. Wu, C. P. Conrad, A. Heuret, C. Lithgow-Bertelloni, S. Lallemand, Reconciling strong slab pull and weak plate bending: The plate motion constraint on the strength of mantle slabs. Earth Planet. Sci. Lett. 272, 412-421 (2008).
- B. H. Hager, Subducted slabs and the Geoid: Constraints on mantle rheology and flow. J. Geophys. Res. 89, 6003-6015 (1984).
- X. Liu, S. Zhong, The long-wavelength geoid from three-dimensional spherical models of thermal and thermochemical mantle convection. J. Geophys. Res. Solid Earth 120, 4572–4596 (2015).
- M. Rudolph, V. Lekić, C. Lithgow-Bertelloni, Viscosity jump in earth's mid-mantle. Sci. 350, 1349–1352 (2015).
- B. Steinberger, A. R. Calderwood, Models of large-scale viscous flow in the earth's mantle with constraints from mineral physics and surface observations. *Geophys. J. Int.* 167, 1461–1481 (2006).

Adjoint-Based Derivative Computation. We use an adjoint method to compute gradients of J, which are needed to iteratively compute \mathbf{m}_{map} as the minimizer of Eq. 5. With this adjoint method, the gradient of J is computed as

$$\delta_{\mathbf{m}}J(\mathbf{m}) = C_{\text{prior}}^{-1}(\mathbf{m} - \mathbf{m_0}) + \int_{\Omega} 2\frac{d\eta(\mathbf{x}, \mathbf{7}, \dot{\varepsilon}_{\parallel}(\mathbf{u}), \mathbf{m})}{d\mathbf{m}} \dot{\varepsilon}(\mathbf{u}) : \dot{\varepsilon}(\mathbf{v}) d\mathbf{x}, \quad [6]$$

where η is the viscosity from Eq. ${\bf 2}$ that depends on ${\bf x}$, the temperature T, the second invariant of the strain rate $\dot{{\bf e}}_{||}$ and the present parameters ${\bf m}$. Moreover, ${\bf u}$ is the solution of Eq. ${\bf 1}$ and ${\bf v}$ the adjoint velocity, which is computed as solution to an adjoint Stokes system. For derivation and details, we refer to refs. 38 and 39. The maximum a posterior ${\bf m}_{\rm map}$ is computed using a Newton-type method with the adjoint-based gradient Eq. ${\bf 6}$ and the Hessian approximated by the Broyden–Fletcher–Goldfarb–Shanno (BFGS) algorithm (69). The Hessian at the MAP point, whose inverse is used as a covariance approximation needs to be of higher accuracy than a BFGS approximation. Therefore, it is computed column-by-column using second-order sensitivity analysis.

Data, Materials, and Software Availability. Model data and postprocessing scripts have been deposited to Zenodo (https://doi.org/10.5281/zenodo. 11697180) (70). All other data are included in the article and/or *SI Appendix*.

ACKNOWLEDGMENTS. Computations were carried out on the NSF-supported Stampede-2 and Frontera supercomputers at the Texas Advanced Computer Center under allocations TG-EAR160027, TG-DPP130002, and FTA-SUB-CalTech, and Anvil at Purdue University (Rosen Center for Advanced Computing) under allocations EAR-160027. J.H. was further supported by the National Key R&D Program of China through award 2023YFF0806300 and National Natural Science Foundation of China through award 92155307.

Author affiliations: ^aDepartment of Earth and Space Sciences, Southern University of Science and Technology, Shenzhen 518055, China; ^bDepartment of Mathematics, Virginia Tech, Blacksburg, VA 24061; ^cSeismological Laboratory, Division of Geological and Planetary Sciences, California Institute of Technology, Pasadena, CA 91125; and ^dCourant Institute of Mathematical Sciences, New York University, New York, NY 10012

- J. X. Mitrovica, A. M. Forte, Radial profile of mantle viscosity: Results from the joint inversion of convection and postglacial rebound observables. J. Geophys. Res. Solid Earth 102, 2751–2769 (1997).
- S. Panasyuk, B. Hager, Inversion for mantle viscosity profiles constrained by dynamic topography and the geoid, and their estimated errors. Geophys. J. Int. 143, 821–836 (2000).
- W. Mao, S. Zhong, Constraints on mantle viscosity from intermediate-wavelength geoid anomalies in mantle convection models with plate motion history. J. Geophys. Res. Solid Earth 126, e2020JB021561 (2021).
- L. Moresi, M. Gurnis, Constraints on the lateral strength of slabs from three-dimensional dynamic flow models. Earth Planet. Sci. Lett. 138, 15-28 (1996).
- R. G. Gordon, G. A. Houseman, Deformation of Indian Ocean lithosphere: Evidence for a highly nonlinear rheological law. J. Geophys. Res. Solid Earth 120, 4434–4449 (2015).
- L. Alisic, M. Gurnis, G. Stadler, C. Burstedde, O. Ghattas, Multi-scale dynamics and rheology of mantle flow with plates. J. Geophys. Res. Solid Earth 117, B10402 (2012).
- J. Warren, G. Hirth, Grain size sensitive deformation mechanisms in naturally deformed peridotites. Earth Planet. Sci. Lett 248, 438-450 (2006).
- P. Skemer, J. M. Warren, P. B. Kelemen, G. Hirth, Microstructural and rheological evolution of a mantle shear zone. J. Petrol. 51, 43–53 (2010).
- T. V. Gerya, D. Bercovici, T. W. Becker, Dynamic slab segmentation due to brittle-ductile damage in the outer rise. Nature 599, 245–250 (2021).
- 29. R. D. Müller, M. Sdrolias, C. Gaina, W. R. Roest, Age, spreading rates, and spreading asymmetry of the world's ocean crust. *Geochem. Geophys. Geosyst.* **9**, 004006 (2008).
- G. P. Hayes et al., Slab2, a comprehensive subduction zone geometry model. Science 362, 58–61 (2018).
- N. A. Simmons, S. C. Myers, G. Johannesson, E. Matzel, LLNL-G3Dv3: Global P wave tomography model for improved regional and teleseismic travel time prediction. J. Geophys. Res. Solid Earth 117, B10302 (2012).
- D. F. Argus, R. G. Gordon, C. DeMets, Geologically current motion of 56 plates relative to the no-net-rotation reference frame. Geochem. Geophys. Geosyst. 12, Q11001 (2011).
- Y. Ricard, C. Doglioni, R. Sabadini, Differential rotation between lithosphere and mantle: A consequence of lateral mantle viscosity variations. J. Geophys. Res. Solid Earth 96, 8407–8415 (1991)
- M. Gérault et al., The role of slabs and oceanic plate geometry in the net rotation of the lithosphere, trench motions, and slab return flow. Geochem. Geophys. Geosyst. 13, Q04001 (2012).
- J. Rudi, G. Stadler, O. Ghattas, Weighted BFBT preconditioner for Stokes flow problems with highly heterogeneous viscosity. SIAM J. Sci. Comput. 39, S272–S297 (2017).
- J. Rudi, G. Yh Shih, Stadler, Advanced Newton methods for geodynamical models of Stokes flow with viscoplastic rheologies. Geochem. Geophys. Geosyst. 21, e2020GC009059 (2020).

- 37. J. Rudi et al., "An extreme-scale implicit solver for complex PDEs: Highly heterogeneous flow in Earth's mantle" in SC15: Proceedings of the International Conference for High Performance Computing, Networking, Storage and Analysis, J. Kern, J. S. Vetter, Eds. (ACM, 2015), pp. 5:1-5:12.
- V. Ratnaswamy, G. Stadler, M. Gurnis, Adjoint-based estimation of plate coupling in a non-linear mantle flow model: Theory and examples. Geophys. J. Int. 202, 768-786 (2015).
- J. Rudi, M. Gurnis, G. Stadler, Simultaneous inference of plate boundary stresses and mantle rheology using adjoints: Large-scale 2-D models. Geophys. J. Int. 231, 597-614 (2022).
- G. Stadler et al., The dynamics of plate tectonics and mantle flow: From local to global scales. Science 329, 1033-1038 (2010).
- J. Hu, M. Gurnis, J. Rudi, G. Stadler, R. D. Müller, Dynamics of the abrupt change in Pacific Plate
- motion around 50 million years ago. *Nat. Geosci.* **15**, 74–78 (2022).

 T. S. Baumann, B. J. P. Kaus, A. A. Popov, Constraining effective rheology through parallel joint geodynamic inversion. *Tectonophysics* **631**, 197–211 (2014).
- D. Argus, R. Gordon, No-net-rotation model of current plate velocities incorporating plate motion
- model NUVEL-1. Geophys. Res. Lett. 18, 2039-2042 (1991). J. Korenaga, S. I. Karato, A new analysis of experimental data on olivine rheology. J. Geophys. Res.
- Solid Earth 113, B02403 (2008). U. Christensen, Convection with pressure- and temperature-dependent non-Newtonian rheology.
- Geophys. J. Int. 77, 343-384 (1984). K. E. Torrance, D. L. Turcotte, Thermal convection with large viscosity variations. J. Fluid Mech. 47,
- 113-125 (1971). Publisher: Cambridge University Press. D. Li, M. Gurnis, G. Stadler, Towards adjoint-based inversion of time-dependent mantle convection
- with nonlinear viscosity. Geophys. J. Int. 209, 86-105 (2017). J. D. Byerlee, Brittle-ductile transition in rocks. J. Geophys. Res. 73, 4741-4750 (1968).
- W. F. Brace, D. Kohlstedt, Limits on lithospheric stress imposed by laboratory experiments.
- J. Geophys. Res. Solid Earth 85, 6248-6252 (1980). D. Bercovici, A source-sink model of the generation of plate tectonics from non-Newtonian mantle flow. J. Geophys. Res. Solid Earth 100, 2013-2030 (1995).
- 51. H. J. van Heck, P. J. Tackley, Planforms of self-consistently generated plates in 3D spherical geometry. Geophys. Res. Lett. 35, L19312 (2008).
- B. J. Foley, T. W. Becker, Generation of plate-like behavior and mantle heterogeneity from a spherical, viscoplastic convection model. *Geochem. Geophys. Geosyst.* **10**, Q08001 (2009).
- A. Osei Tutu, S. V. Sobolev, B. Steinberger, A. A. Popov, I. Rogozhina, Evaluating the influence of plate boundary friction and mantle viscosity on plate velocities. Geochem. Geophys. Geosyst. 19, 642-666 (2018).
- C. R. Ranero, J. Phipps Morgan, K. McIntosh, C. Reichert, Bending-related faulting and mantle serpentinization at the middle America trench. Nature 425, 367-373 (2003).

- 55. L. H. Rüpke, J. P. Morgan, M. Hort, J. A. Connolly, Serpentine and the subduction zone water cycle Earth Planet. Sci. Lett. 223, 17-34 (2004).
- L. Liu, D. R. Stegman, Segmentation of the Farallon slab. Earth Planet. Sci. Lett. 311, 1-10 (2011).
- D. R. Stegman, R. Farrington, F. A. Capitanio, W. P. Schellart, A regime diagram for subduction styles from 3-D numerical models of free subduction. Tectonophysics 483, 29-45
- E. Di Giuseppe, J. van Hunen, F. Funiciello, C. Faccenna, D. Giardini, Slab stiffness control of trench motion: Insights from numerical models. Geochem. Geophys. Geosyst. 9, Q0201 (2008).
- P. Bird, An updated digital model of plate boundaries. Geochem. Geophys. Geosyst. 4, 1027
- B. A. Buffett, D. B. Rowley, Plate bending at subduction zones: Consequences for the direction of plate motions. *Earth Planet. Sci. Lett.* **245**, 359–364 (2006).
- S. I. Karato, Importance of anelasticity in the interpretation of seismic tomography. Geophys. Res. Lett. 20, 1623-1626 (1993).
- J. Ritsema, A. Deuss, H. Van Heijst, J. Woodhouse, S40rts: A degree-40 shear-velocity model for the mantle from new rayleigh wave dispersion, teleseismic traveltime and normal-mode splitting function measurements. Geophys. J. Int. 184, 1223-1236 (2011).
- T. W. Becker et al., Western US intermountain seismicity caused by changes in upper mantle flow. Nature 524, 458-461 (2015).
- D. B. Rowley, A. M. Forte, Kinematics of the east pacific rise retrodicted from pacific and farallon/nazca subduction-related torques: Support for significant deep mantle buoyancy controlling EPR spreading. J. Geophys. Res. Solid Earth 127, e2020JB021638 (2022).
- M. Chen et al., Lithospheric foundering and underthrusting imaged beneath Tibet. Nat. Commun.
- J. Li, X. Song, Tearing of Indian mantle lithosphere from high-resolution seismic images and its implications for lithosphere coupling in southern Tibet. Proc. Natl. Acad. Sci. U.S.A. 115, 8296-8300 (2018).
- 67. C. Li, R. D. Van Der Hilst, Structure of the upper mantle and transition zone beneath southeast Asia
- from traveltime tomography. *J. Geophys. Res. Solid Earth* **115**, B07308 (2010). Z. Wang, D. Zhao, R. Gao, Y. Hua, Complex subduction beneath the Tibetan plateau: A slab warping model. *Phys. Earth Planet. Inter.* **292**, 42–54 (2019).
- J. Nocedal, S. J. Wright, Numerical Optimization (Springer Verlag, Berlin, Heidelberg, New York, ed. 2, 2006).
- J. Hu, J. Rudi, M. Gurnis, G. Stadler, Constraining Earth's nonlinear mantle viscosity using plateboundary resolving global inversions. Zenodo. https://doi.org/10.5281/zenodo.11697180. Deposited 16 June 2024.